8A.6

MESOCYCLONE AND RFD EVOLUTION IN SIMULATED SUPERCELL STORMS WITH VARYING WIND PROFILES

Matthew S. Van Den Broeke
Jerry M. Straka
University of Oklahoma, Norman, Oklahoma

Erik Rasmussen
Rasmussen Systems, Mesa, Colorado

1. THEORETICAL OVERVIEW AND PURPOSE

Many observational and modeling studies have focused on mesocyclone evolution in supercells. Adlerman and Droegemeier (2005) developed a parameter space of hodograph shapes, and tested mesocyclone sensitivity to these environmental wind shear variations. Three types of mesocyclone evolution were identified: steady (non-cycling), occluding cyclic, and non-occluding cyclic. Decreased sensitivity to hodograph shape and model resolution has been documented for supercells in simulations with strong vertical wind shear (Gilmore et al. 2004a).

Most supercell modeling studies have historically included liquid-only microphysics. A recent study showed significant differences in updraft strength, surface precipitation outcome, and cold pool strength in simulations identical except for choice of microphysics (Gilmore et al. 2004b). Ice-inclusive microphysics produced stronger updrafts due to greater latent heat release. As expected from past studies (e.g. Srivastava 1987), cold pool strength was also greater, which may have nontrivial effects on the inflow-outflow balance near the mesocyclone.

For this study, a subset of twelve hodographs from Adlerman and Droegemeier (2005) were chosen, including three full-circle, three three-quarter-circle, and six half-circle wind profiles. For each hodograph, a simulation was run using liquid-only microphysics, similar to what was done in Adlerman and Droegemeier's study, and another simulation was run with ice-inclusive microphysics. Mesocyclone behavior from the liquid-only runs was compared with the results of Adlerman and Droegemeier (2005), then the liquid-only and ice-inclusive simulations were compared. Differences were sought between different hodograph shapes and varying magnitude of environmental shear. Microphysical differences were examined among the ice-inclusive simulations, in an attempt to link environmental shear, the resultant microphysical environment, and consequent effects on the cold pool, with potential implications for surface vertical vorticity concentration.

* *Corresponding author address*: Matthew S. Van Den Broeke, School of Meteorology, 120 David L. Boren St., Norman, OK 73072
E-mail: Matthew.VanDenBroeke@OU.edu

2. METHODOLOGY

With the goal of determining effects of varying shear on microphysical distributions in supercells, a subset of twelve wind profiles from Adlerman and Droegemeier's (2005) parameter space was chosen (Fig. 1). Simulations were selected such that they covered the parameter space well, while favoring wind profiles near the edge of two mesocyclone cycling types in Adlerman and Droegemeier's study. This was done to test sensitivity of cycling type to choice of microphysics.

The model used was the three-moment, non-hydrostatic, three-dimensional, compressible Straka Atmospheric Model (SAM) with a time step of 1s and horizontal resolution of 250m. Model output files were generated every 5 min. Vertical resolution stretched from 155m near the surface to 520m at 20km, with a lowest level 75m above the surface. The Weisman and Klemp (1982) thermodynamic environment was utilized for all simulations, and a 3K circular warm bubble was used to initiate convection. This thermodynamic profile is more stable than was used in Adlerman and Droegemeier (2005), possibly leading to differences in cycling behavior as discussed later.

Microphysics were either liquid-only, as in Soong and Ogura (1973) and Klemp and

Wilhelmson (1978), and identical to the scheme used in Adlerman and Droegemeier (2005), or ice-inclusive. The ice scheme used nine species of ice-phase hydrometeors, including two hail categories, four types of ice crystals, snow aggregates, frozen drops, and graupel. It also contained drizzle and three formation processes for rain. SAM output files were visualized using iMRV, an IDL iTool for meteorological visualization created and supported by Erik Rasmussen at Rasmussen Systems.

Once graphics were created, cyclic behavior of the mesocyclone was examined for each simulation. Graphics were constructed at each 5 min interval containing vertical velocity and vertical vorticity, and changes in updraft and vorticity distributions were used to determine if the mesocyclone was steady, cyclic occluding, or cyclic non-occluding. Maximum surface vertical vorticity at each interval was recorded, and at the time of simulation maximum surface vertical vorticity, plots were constructed of surface potential temperature distribution and the vertical and horizontal wind components. For ice-inclusive simulations, distributions of different types of rain and hail and other frozen particles were plotted at the time of maximum surface vorticity. Various wind, vorticity, and microphysical characteristics of the simulations were plotted on the wind profile parameter space.

3. COMPARISON WITH PAST WORK

Results were compared with past work to ensure the SAM was producing similar results. Since the wind profiles were taken from Adlerman and Droegemeier (2005), mesocyclone behavior was compared to these simulations. Simulations with liquid-only microphysics were compared, as these were most similar to those of Adlerman and Droegemeier's study.

For liquid-only simulations in the SAM, three modes of mesocyclone cyclicality were observed (Fig. 2). These modes were described and drawn without looking at the modes as described in Adlerman and Droegemeier (2005), but completely agreed with their results. This agreement between model-produced types of mesocyclone cyclicality raised confidence in the SAM's ability to produce similar evolution as seen in prior modeling studies.

Mesocyclone cycling modes are shown on the parameter space of wind profiles for Adlerman and Droegemeier's study (Fig. 3a) and for the liquid-only simulations in this study (Fig. 3b). These results agreed quite well. The significant difference was an expansion of the area of occluding cyclic mesocyclogenesis with the SAM—one wind profile producing a steady mesocyclone in Adlerman and Droegemeier's study produced an occluding cyclic mesocyclone in the SAM, while several simulations changed from non-occluding cyclic to occluding cyclic.

Though these results agreed relatively well, reasons were briefly sought as to why the SAM model produced a higher number of occluding cyclic storms. While the wind profile was identical, convective available potential energy (CAPE) was 3777 J kg^{-1} in Adlerman and Droegemeier's (2005) simulations but only approximately 2200 J kg^{-1} in our simulations. Lower CAPE, all else equal, should lead to lower updraft speed, which would reduce total mass fallout of hydrometeors from the updraft (e.g. Gilmore et al. 2004b). This may slightly reduce cold pool strength via less precipitation loading, and possibly via less evaporation and melting. Given the propensity of liquid-only microphysics to produce unrealistically strong cold pools (e.g. compared to observations, as in Markowski et al. 2002), a slight cold pool warming (via less evaporation) or slightly lesser downward motion in the downdrafts (via less loading) could be expected to produce a different inflow-outflow balance. Since this balance between unstable storm-relative inflow and surging cold outflow determines much about mesocyclone behavior, a 40% decrease in environmental CAPE may change mesocyclone behavior to include more cyclic occluding storms.

4. COMPARISON OF ICE AND LIQUID MICROPHYSICS

Ice and liquid microphysics produced very different patterns of mesocyclone cyclicality overall. *Steady non-cyclic storms did not occur with ice-inclusive microphysics for this choice of CAPE* (Fig. 4), while non-occluding cyclic storms, which had not previously occurred in this subset of Adlerman and Droegemeier's parameter space (2005) became the dominant mode of mesocyclone behavior. Occluding cyclic storms occupied two separate regimes, one characterized by low shear with nearly all hodograph shapes, and another at strong shear mostly with hodograph shapes not included in our present subset. In following subsections, we examine the simulations categorized by hodograph shape.

4.1 *Full-Circle Hodographs*

The most striking difference occurred with full-circle hodographs (Figs. 3b, 4). With liquid-only microphysics, storms were only briefly supercellular and possessed a steady non-cycling mesocyclone. After a short time as a supercell, the cold pool of these storms surged eastward. An extensive wall of updraft resulted, with rapid transition to a squall line. *With ice-inclusive microphysics, however, storms were maintained as supercells* with a generally continuous, well-defined mesocyclone. The mesocyclone in these storms tended to build northward along the rear-flank downdraft (RFD) outflow, with a new surface center of vertical vorticity developing northward of its prior location. This was consistent with non-occluding cyclic behavior, and occurred given all amounts of environmental wind shear tested.

4.2 *Three-Quarter-Circle Hodographs*

Supercells in environments with three-quarter-circle hodographs consistently contained occluding cyclic mesocyclones with liquid-only microphysics. While this was also true for low environmental shear given ice-inclusive microphysics, a transition to non-occluding cyclic behavior occurred as shear increased. This transition appeared to occur with a hodograph radius of about 19 m/s. Around this boundary, mesocyclones contained distinct periods of time in which occluding and non-occluding cyclic behavior were dominant.

4.3 *Half-Circle Hodographs*

With liquid-only microphysics, most supercells given half-circle hodographs produced occluding cyclic mesocyclones except at very low shear. Half the simulations with ice-inclusive microphysics produced the same occluding cyclic behavior, while the remaining half contained non-occluding cyclic mesocyclones. Non-occluding cyclic behavior was generally dominant for moderate environmental shear. Simulations with very low and high shear were able to produce a better-focused westerly component in the RFD, leading to occlusion.

The goal of following sections will be to further explore differences between ice and liquid simulations, and to explain some of these differences by exploring the effects of varying shear on hydrometeor distributions. Given different hydrometeor distributions, link will be sought between varying microphysics and storm behavior.

5. COMPARISON OF SELECTED SIMULATION CHARACTERISTICS

A number of variables were plotted on the wind profile parameter space, related to updraft strength and the timing and efficiency of vertical vorticity concentration. These fields were compared for ice and liquid simulations, and some brief attempts were made to explain differences.

Simulations were examined from 3000s – 9000s (50 min – 2.5 hrs), so for model output each 5 min, twenty-one times were available for each simulation. Number of these output steps with updraft magnitude > 15 ms^{-1} at 1000m above the surface were plotted on the parameter space for ice and liquid (Fig. 5). The most notable difference overall was the larger number of steps with strong updraft in the liquid-only simulations. This difference seemed to be caused by the *stronger cold pools in the liquid-only simulations, which caused cold outflow to surge eastward and strengthen the updrafts into which they moved*. In full-circle simulations, storms rapidly evolved into squall lines, which had strong updraft regions along their leading edges. For other hodograph shapes, a greater proportion of liquid-only simulations had some steps with updraft exceeding 15 m/s. This was apparently also related to a stronger cold pool leading to a markedly stronger westerly component in the RFD of those storms.

Time of the first strong surface (75m) vertical vorticity maximum was plotted on the parameter space (Fig. 6a), along with the difference between ice and liquid simulations (Fig. 6b). A strong maximum, for this purpose, was defined as a temporal maximum at least 50% as strong as the simulation maximum value. Both sets of simulations showed a trend toward *increasing time to concentrate vertical vorticity at the surface as shear increased*; this trend was especially evident in the liquid-only simulations. This result is consistent with past research, in which slowing of mesocyclone cycling has been observed as environmental shear increases (e.g. Brooks et al. 1994). The ice-inclusive simulations did not show this trend as clearly, though it was still present. The difference field between ice and liquid simulations clearly showed *less time for ice-inclusive simulations to concentrate surface vertical vorticity at high shear*, though it took slightly longer at low shear. The mesocyclones of

storms in ice-inclusive simulations, especially at higher shear, tended to be conducive to more rapid development of strong RFDs, which formed zones of strong vorticity to their north.

The average time between successive surface vertical vorticity maxima was calculated, and the difference field between ice and liquid simulations was plotted on the parameter space (Fig. 7). For all hodograph shapes examined here, ice microphysics produced storms which cycled faster, relative to the liquid-only storms, as shear increased. As shear increased, the ice-inclusive storms continued to produce well-defined mesocyclones with periodic strong RFDs at about the same interval. The liquid-only simulations, however, showed a tendency toward more linear structures, leading to fewer surface vorticity maxima.

A difference field of simulation maximum surface vertical vorticity was plotted on the parameter space (Fig. 8). Though there were exceptions, a few trends were noted. *Magnitude of maximum vorticity was nearly always larger for the ice-inclusive simulations*—these storms were able to produce a stronger surface vortex for a given environmental shear. Better-developed mesocyclones on average in the ice-inclusive simulations, consisting of well-defined updraft and RFD regions collocated with enhanced vertical vorticity at midlevels, may be partially responsible for this trend. Also, the magnitude of this difference typically increased as environmental shear increased. This suggests the ice-inclusive storms may better utilize increasing environmental shear to develop and maintain more intense surface vortices.

As a measure of a storm's efficiency at repeatably concentrating vertical vorticity at the surface, maximum surface vertical vorticity was summed across all twenty-one model output times. A difference field of this variable was plotted on the wind profile parameter space (Fig. 9). Neither ice nor liquid simulations tended to dominantly contain higher summed surface vorticity. Readily apparent, however, was a trend toward higher *relative* summed vorticity in the ice-inclusive simulations for higher shear. This reinforces a previous conclusion—*ice-inclusive storms seem better able to utilize increasing environmental shear in the processes that generate and maintain surface vortices*.

6. DIFFERENCES IN RFD STRENGTH AND THE ROLE OF ICE MICROPHYSICS

RFD strength varied significantly between simulations, so some quantitative comparisons are made between RFD wind and temperature fields. Microphysical distributions are explored to shed some light on why storms may evolve differently. For the purpose of this work, the RFD was defined as the small-scale region of downdraft closely associated with the mesocyclone, and typically located on the south or southwest side of the mesocyclone in or near the echo appendage.

6.1 *Quantitative Comparisons of RFD Strength*

Surface vertical vorticity maxima, in all simulations but especially in ice-inclusive simulations, were associated with a surge of RFD westerlies just south of the surface vortex. This westerly surge was defined as a small-scale region of storm-relative west-to-east flow generally in the southwest portion of the mesocyclone. Magnitude of westerlies in this RFD surge was determined for each simulation and the approximate difference field plotted on the wind profile parameter space (Fig. 10). Overall, a stronger RFD westerly component was present in the liquid-only simulations, apparently the result of those storms having stronger cold pools to the west of the updraft region. The notable exception was with full-circle hodographs, in which ice-inclusive storms typically had a stronger RFD surge. This seemed a result of the more defined mesocyclone structure in these storms compared to their liquid-only counterparts, with distinct updraft and RFD regions collocated with enhanced vertical vorticity. The full-circle hodograph with 25 ms^{-1} radius was the exception—the liquid-only simulation with this profile produced a powerful squall line with exceptional westerly winds behind the outflow boundary, leading to an RFD westerly surge of 50 ms^{-1}, the strongest seen in any simulation.

Potential temperature gradient across the RFD boundary was plotted on the wind profile parameter space (Fig. 11). Most strikingly, *this gradient for liquid-only storms averaged twice as strong*. The RFD tended to be uniformly cool for most liquid-only simulations, with a few warmer cases among half-circle hodographs. Patterns were a little different for ice-inclusive storms—full-circle and half-circle hodographs tended to produce relatively cool RFDs, while three-quarter-circle hodographs produced warmer RFDs, relative to the entire parameter space.

6.2 *Effects of Varying Shear on Microphysical Distributions*

Microphysical reasons for the noted differences in RFD strength and mesocyclone organization were sought between ice-inclusive storms. For these investigations, mixing ratios of hail, other frozen particles, and rain from several sources were plotted on the wind profile parameter space. A few associations were discovered between RFD strength and hydrometeor distributions, and a few significant microphysical differences were found between storms forming with different wind profiles.

Maximum hail mixing ratios at 1000m averaged 25% to 60% higher for full-circle hodographs. Also, hail tended to be confined more to the storm core in half-circle simulations, while it tended to spread southward and wrap around the west side of the mesocyclone in full-circle simulations (Fig. 12). *The higher hail content coupled with a slightly different spatial hail distribution in the full-circle simulations likely contributed to stronger RFD westerly components in those simulations*, owing to cooling associated with melting.

Likewise, maximum graupel mixing ratio was typically at least double for full-circle hodographs. Similar to hail, at 1000m the graupel distribution in storms with full-circle hodographs was also typically located farther south, closer to the echo appendage. Larger graupel concentrations alone should produce stronger downdrafts (e.g. Srivastava 1987), though the different spatial distribution of smaller frozen particles may also contribute to the stronger RFDs observed in full-circle simulations.

Increased hail and graupel mixing ratios in some storms may be related to seeding potential. For full-circle hodographs, ice particles would remain nearer the updraft and therefore have a better chance of seeding new areas with ice nuclei. Similarly, *stronger shear was generally found to yield higher mixing ratios of ice-phase particles*. At first this may not seem likely, as stronger shear would remove particles from the updraft region and reduce seeding potential, but a few mechanisms exist which may contribute to the observed pattern. Ice particles from nearby storms would be more likely to seed a given storm if shear were increased, assuming more efficient particle advection. Also, a past study has found increased hydrometeor production with stronger updrafts (Gilmore et al. 2004a). To a point, stronger updrafts were noted with increasing environmental shear, likely as increased dynamic effects added to the updraft strength.

A possible further microphysical contributor to mesocyclone organization is the dominance of certain processes leading to rain formation. In the SAM, rain mixing ratio is calculated for drops formed via melting of graupel, shedding from hail, and via warm rain processes (collision-coalescence). Rain mixing ratio due to melting and shedding was quite similar between most simulations, with values only varying by 100% - 200%. *Warm rain, however, varied by up to four orders of magnitude between the simulations.*

Warm rain typically occurred on the southwest side of the echo appendage, in an updraft region on the west side of the mesocyclone (Fig. 13). The energy budget of warm rain differs fundamentally from that of rain formed by ice processes—most importantly, when warm rain is falling and evaporating, it cools the column less than rain falling with ongoing melting. Large differences have been found in resulting downdraft strength in an idealized numerical downdraft simulation (Srivastava 1987). Thus, *it could be expected that downdrafts formed in a warm rain regime would be weaker than downdrafts formed from mixed-phase precipitation*.

In this study, the amount of rain produced via warm rain processes varied significantly across the wind profile parameter space. *Nearly no warm rain was produced with full-circle hodographs, while greater warm rain production occurred with increasing environmental shear for all hodograph shapes* (Fig. 14). Both observations may be related to the likelihood of seeding. With full-circle hodographs, particles remain in the updraft vicinity, so any ice particles present would have a higher chance of providing ice nuclei to younger, warmer segments of the updraft. The level at which particles freeze would likely be lower in these environments. In the case of stronger shear, ice particles should leave the updraft vicinity more readily via advection, so seeding would become less likely and warm rain processes would be able to dominate a larger, deeper portion of the updraft column, especially its upshear side.

Though not yet shown conclusively, it is suspected that the dominance of warm rain processes on the southwest side of the mesocyclone may influence RFD temperature characteristics. If warm rain processes occupy much of the updraft, the RFD might be warmer, given less melting. If warm rain was uncommon or absent, as in full-circle hodographs or at low

shear, the RFD might be cooler. These contributions to RFD temperature may be small, especially in higher-shear regimes, and may not be well-correlated to tornadogenesis potential.

7. *Conclusions*

The SAM was found to yield similar mesocyclone behavior as seen in a past study with liquid-only microphysics, though the 40% decrease in CAPE yielded more cyclic occluding storms. Ice-inclusive microphysics yielded quite different results—no non-cyclic storms were noted, and non-occluding cyclic storms occupied much of the wind profile parameter space with moderate environmental shear.

With ice-inclusive microphysics, full-circle hodographs were found to yield well-organized and persistent supercells, with little tendency toward linear convection as in liquid-only simulations. Three-quarter-circle hodographs yielded occluding cyclic behavior with weaker shear and non-occluding cyclic behavior with stronger shear. Half-circle hodographs produced variable, but cyclic, mesocyclone behavior.

Cold pools averaged twice as cold in the liquid-only simulations, leading to eastward-surging storm-relative surface winds, stronger updrafts, and a tendency toward linear convective organization. As environmental shear increased, storms took longer to concentrate vertical vorticity near the surface, though this effect was less with ice-inclusive microphysics. Overall, ice-inclusive storms were better able to utilize increasing environmental shear in processes producing and maintaining strong surface vortices. Thus, both magnitude of maximum surface vertical vorticity and magnitude of summed surface vertical vorticity was higher in ice-inclusive simulations at higher shear.

The RFD was marked by a stronger potential temperature gradient in the liquid-only simulations, and contained a stronger westerly component on average. Among the ice-inclusive simulations, full-circle hodographs contained strong RFD westerly components. Greater hail and graupel mixing ratios in those simulations, along with an altered spatial distribution of ice-phase particles and decreased warm rain production, appeared to contribute. Overall, strong shear produced higher concentrations of ice-phase particles, possibly owing to stronger updrafts. Warm rain production increased with increasing shear within a given hodograph shape, and was nearly absent from simulations with full-circle hodographs. Thus, seeding by ice particles near the updraft may be vitally important to downdraft strength in this region.

8. *References*

Adlerman, E. J., and K. K. Droegemeier, 2005: The dependence of numerically simulated mesocyclogenesis upon environmental vertical wind shear. *Mon. Wea. Rev.*, **133**, 3595 – 3623.

Brooks, H. E., C. A. Doswell, and R. B. Wilhelmson, 1994: The role of midtropospheric winds in the evolution and maintenance of low-level mesocyclones. *Mon. Wea. Rev*., **122**, 126 – 136.

Gilmore, M. S., J. M. Straka, and E. N. Rasmussen, 2004a: Precipitation and evolution sensitivity in simulated deep convective storms: comparisons between liquid-only and simple ice and liquid phase microphysics. *Mon. Wea. Rev.*, **132**, 1897 – 1916.

Gilmore, M. S., J. M. Straka, and E. N. Rasmussen, 2004b: Precipitation uncertainty due to variations in precipitation particle parameters within a simple microphysics scheme. *Mon. Wea. Rev.*, **132**, 2610 – 2627.

Klemp, J. B., and R. B. Wilhelmson, 1978: The simulation of three-dimensional convective storm dynamics. *J. Atmos. Sci.*, **35**, 1070 – 1096.

Markowski, P., J. M. Straka, E. N. Rasmussen, 2002: Direct surface thermodynamic observations within the rear-flank downdrafts of nontornadic and tornadic supercells. *Mon. Wea. Rev.*, **130**, 1692-1721.

Srivastava, R. C., 1987: A model of intense downdrafts driven by the melting and evaporation of precipitation. *J. Atmos. Sci.*, **44**, 1752 – 1774.

Soong, S., and Y. Ogura, 1973: A comparison between axisymmetric and slab-symmetric cumulus cloud models. J. Atmos. Sci., **30**, 879 – 893.

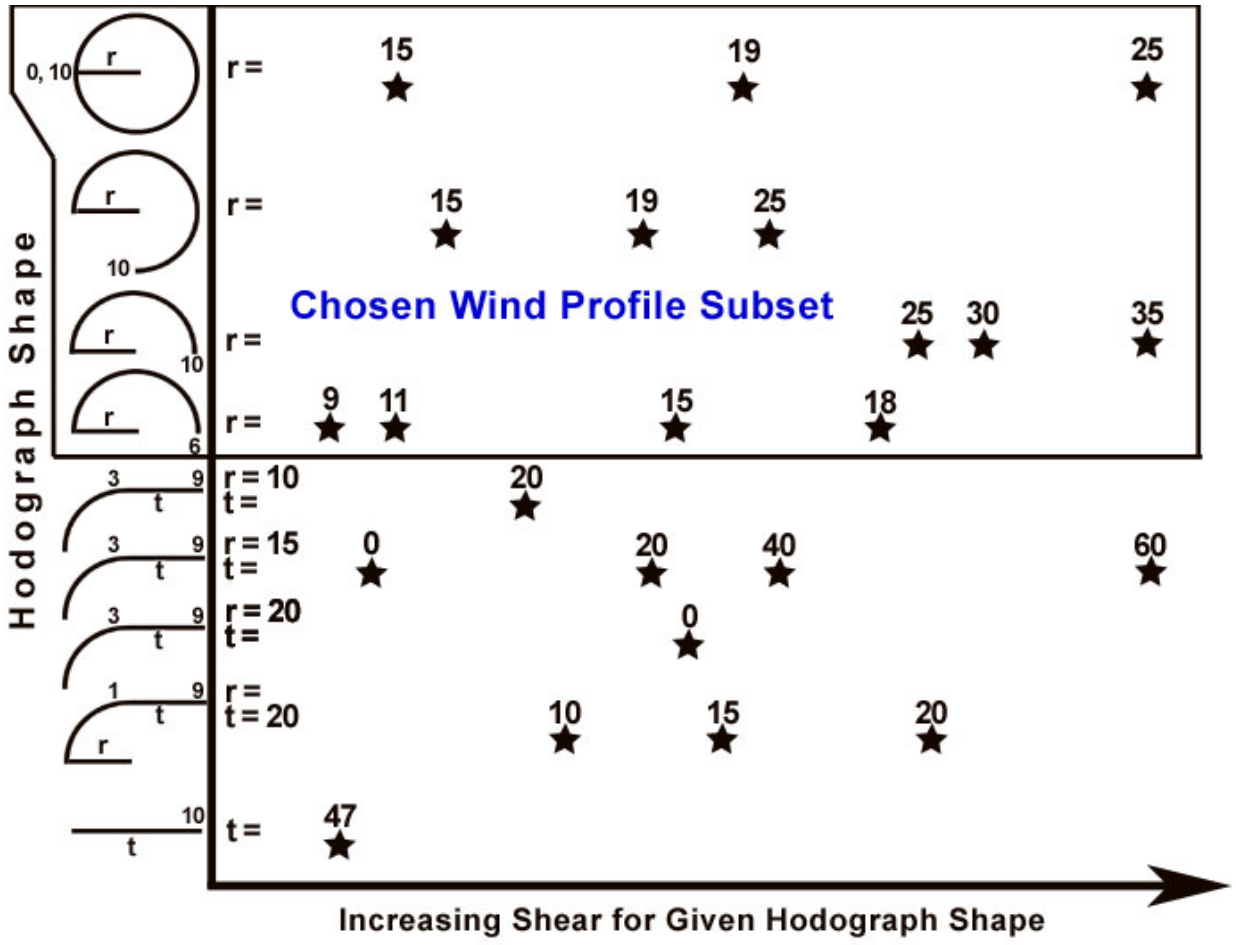

Figure 1: The chosen subset of wind profiles from Adlerman and Droegemeier (2005), consisting of full-circle, three-quarter-circle, and half-circle hodographs. Stars represent individual wind profiles, for which both liquid-only and ice-inclusive simulations were completed. The number above each star represents wind profile radius in ms^{-1} for all simulations in the chosen subset, and tail length in ms^{-1} for most of the other wind profiles.

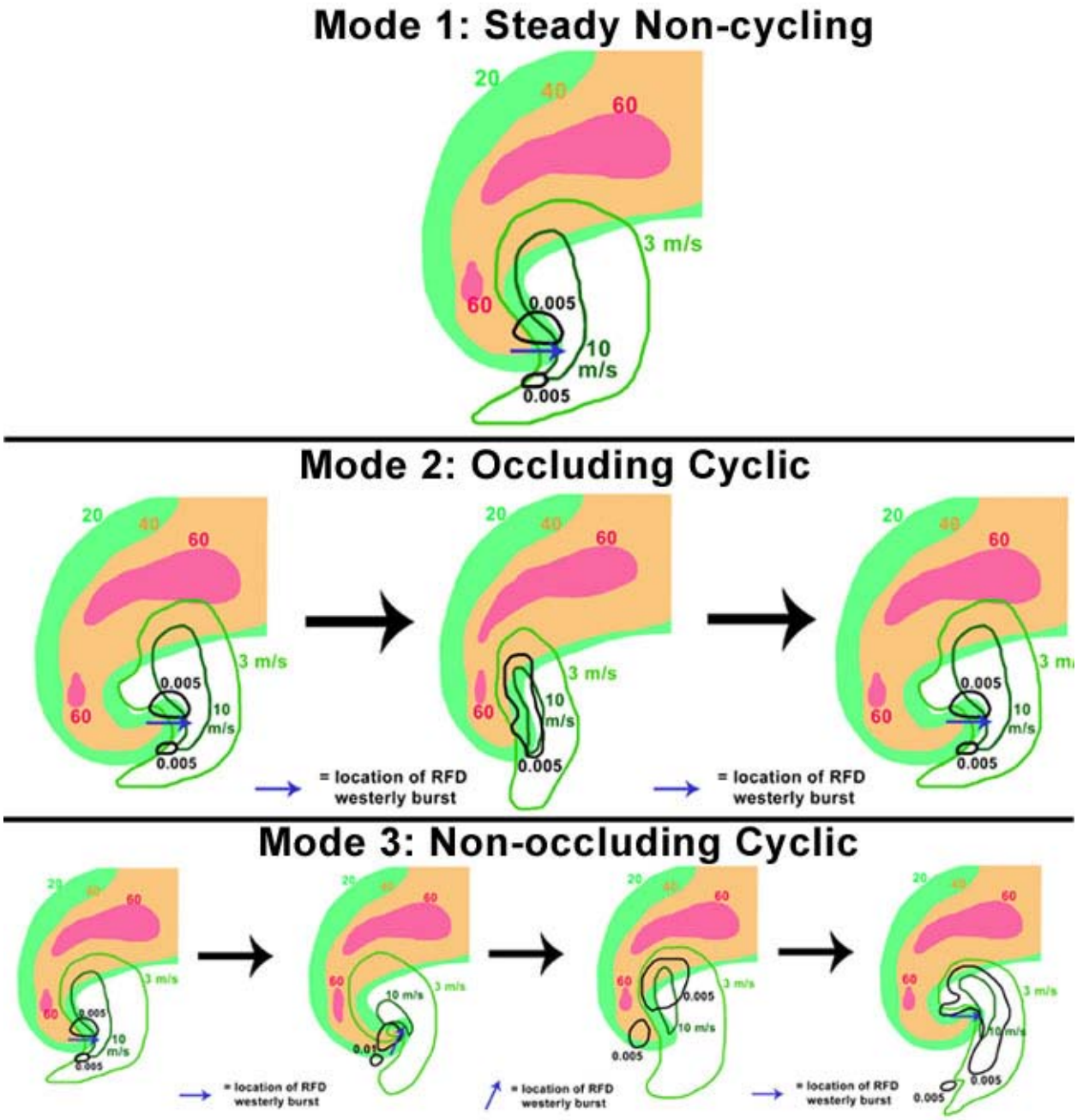

Figure 2: Schematics of three cycling modes observed in simulated storms in the SAM, corresponding to the three modes observed by Adlerman and Droegemeier (2005). Color shading represents 1000-m reflectivity factor in dBZ, light green contour represents 1000-m updraft of 3 ms^{-1}, dark green line represents 1000-m updraft of 10 ms^{-1}, and black contours represent 1000-m vertical vorticity of 0.005. For step two of the non-occluding cyclic process, black contour is 1000-m vertical vorticity of 0.01. In all schematics, blue arrows show the location of a surge of enhanced westerlies associated with the RFD.

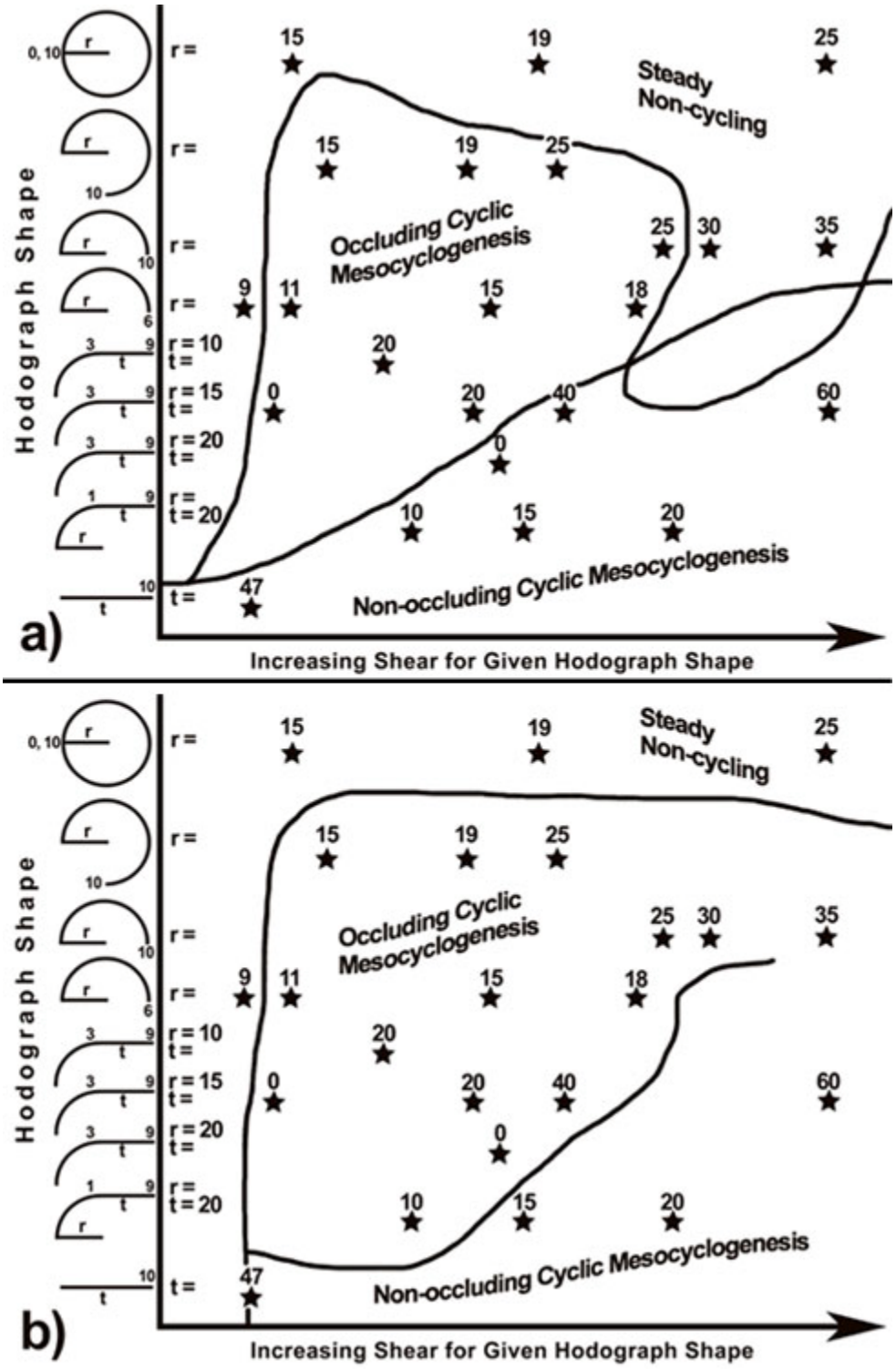

Figure 3: Mesocyclone cycling modes observed in a) the study of Adlerman and Droegemeier (2005), and b) this study, with liquid-only microphysics. Simulations are labeled on the parameter space as described in Fig. 1. Lines denote approximate boundaries of observed cycling types, schematics of which are presented in Fig. 2.

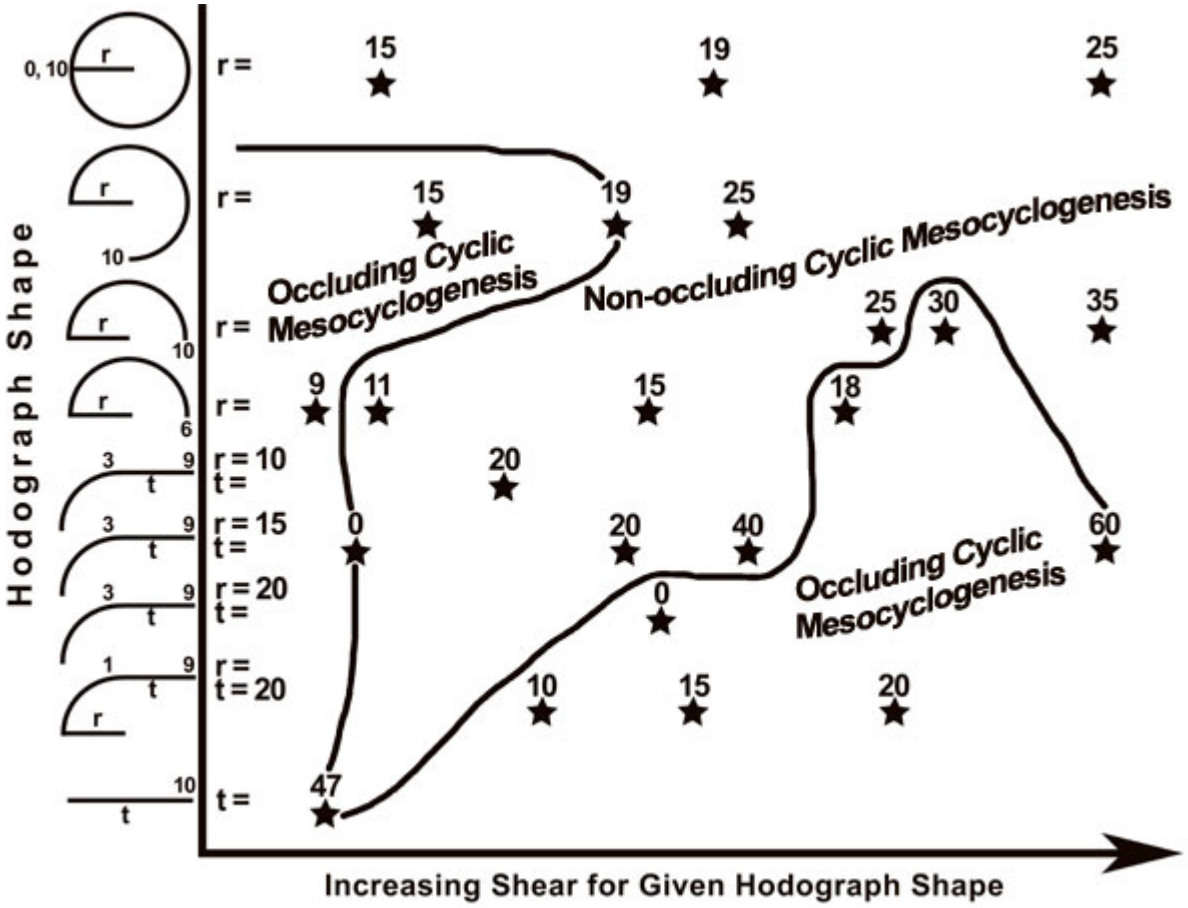

Figure 4: Mesocyclone cycling modes observed in this study with ice-inclusive microphysics. Simulations are labeled on the parameter space as described in Fig. 1. Lines denote approximate boundaries of cycling types, schematics of which are presented in Fig. 2.

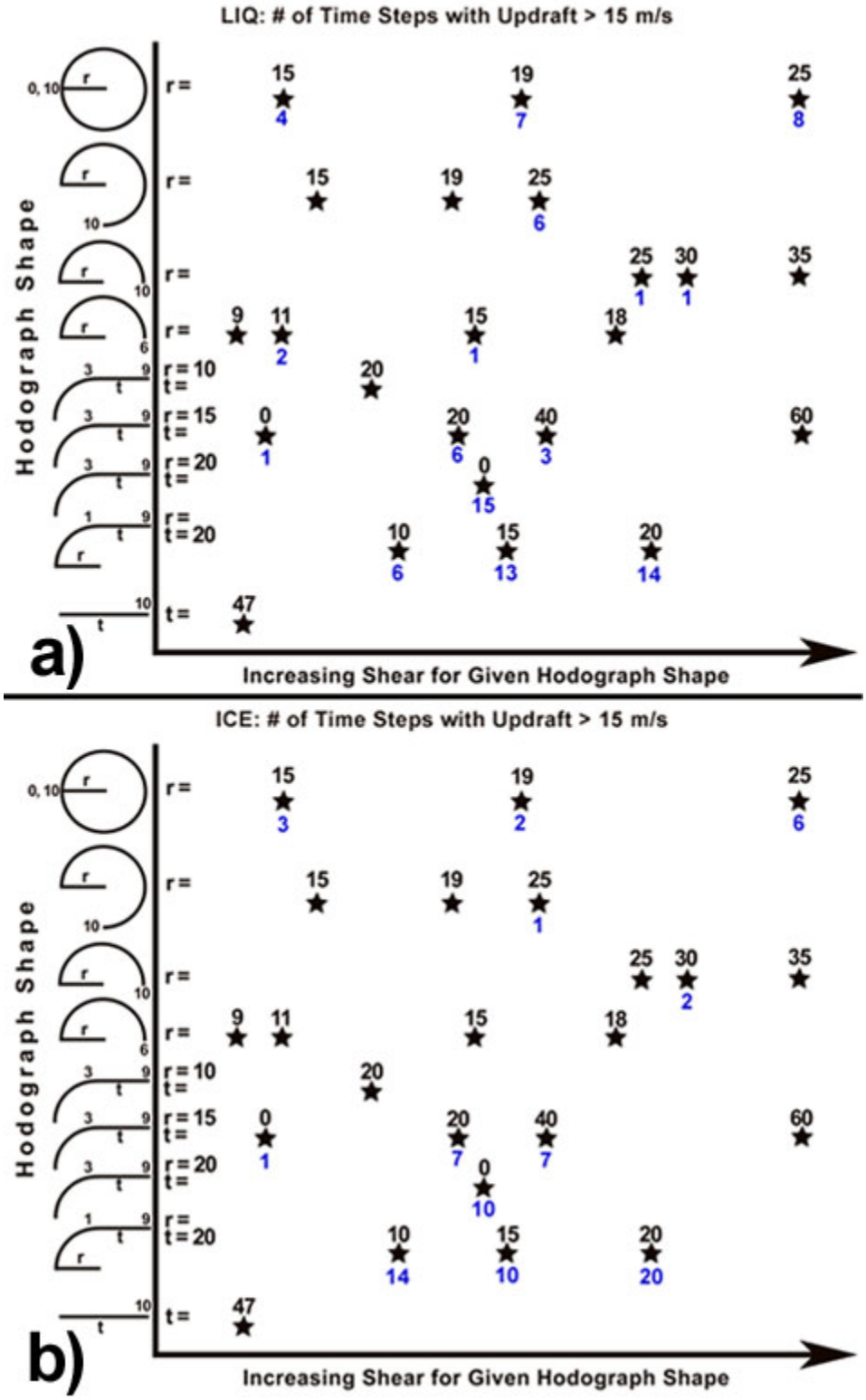

Figure 5: Number of model output steps which had maximum updraft at 1000m of at least 15 ms^{-1} for a) the liquid-only simulations, and b) the ice-inclusive simulations. Simulations are denoted as described in Fig. 1, and number of steps is shown by the blue number below each star. If no number is present, no steps contained an updraft this strong at 1000m.

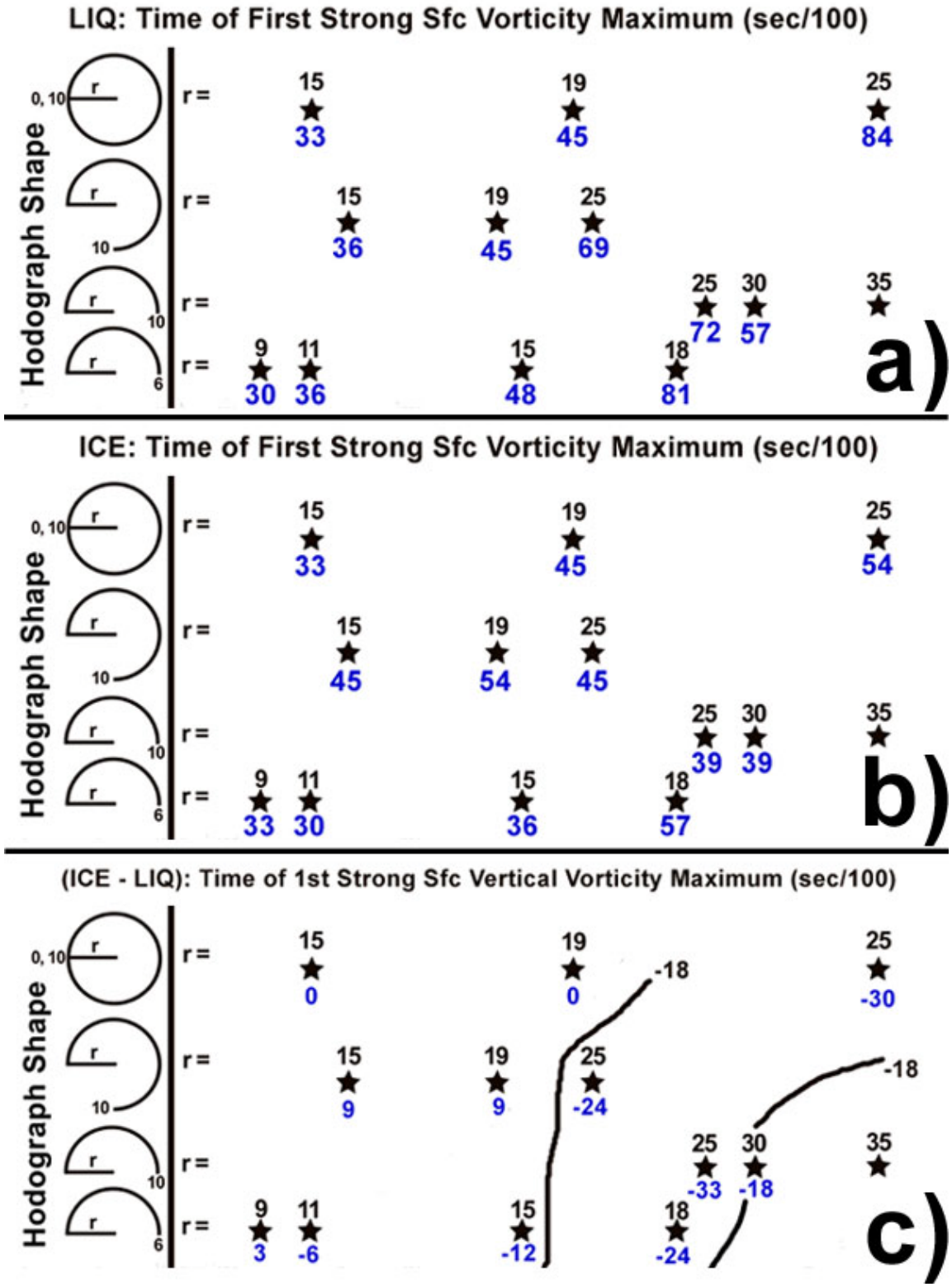

Figure 6: Time of the first surface vertical vorticity maximum with magnitude at least 50% of the simulation maximum. a) is for the liquid-only simulations, b) is for the ice-inclusive simulations, and c) shows the difference field (ice minus liquid) for this variable. Times, denoted in blue, are number of seconds since model initialization divided by 100 (e.g. 5400s = 54). The -1800s contour is highlighted in (c).

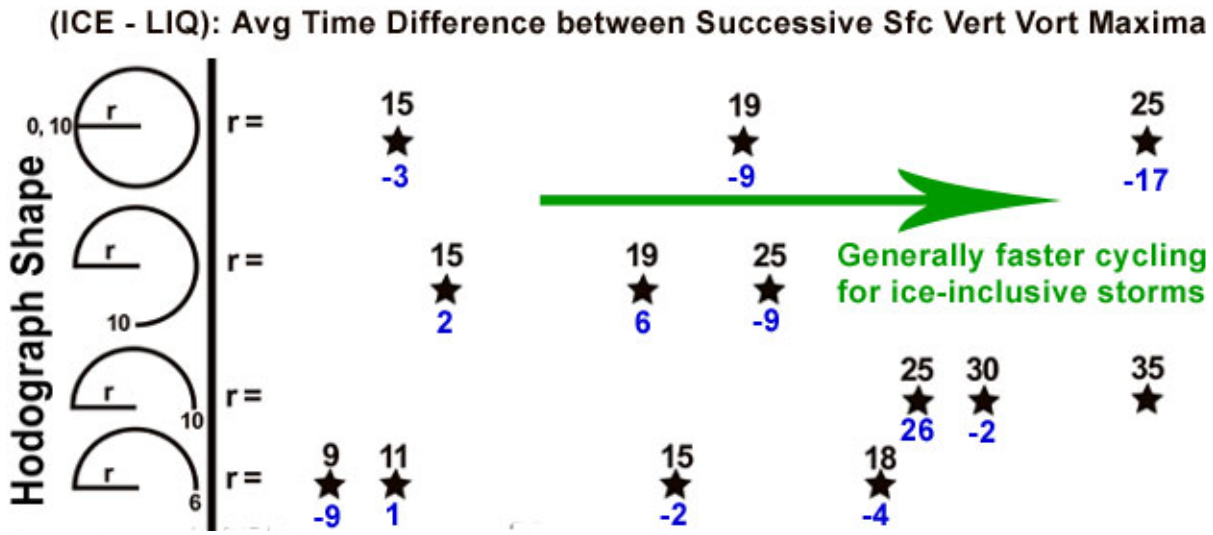

Figure 7: Average difference in time between successive surface vertical vorticity maxima, calculated as ice minus liquid values. The blue number below each simulation represents this difference in minutes.

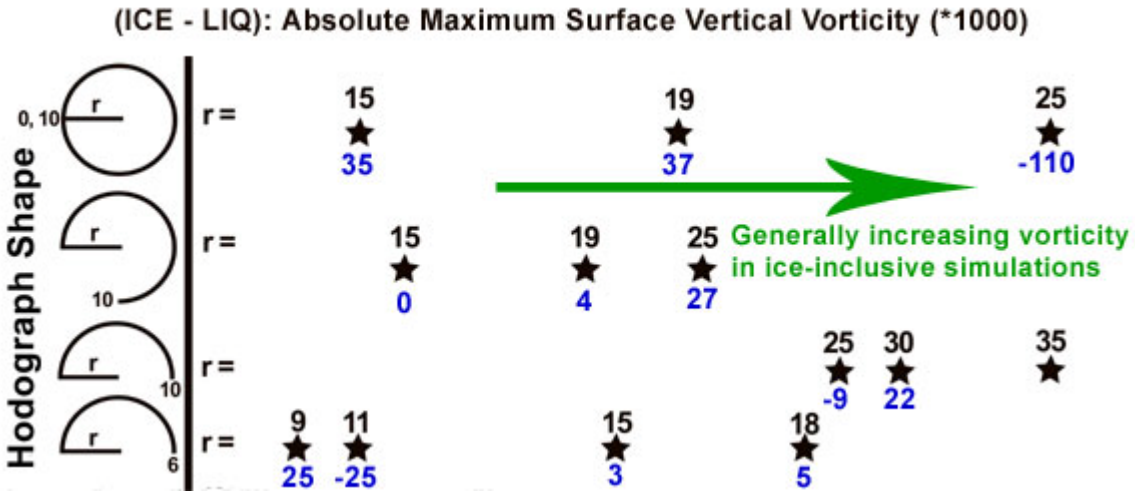

Figure 8: Difference in maximum surface vertical vorticity between ice and liquid simulations, represented by the blue number below each simulation. This number represents the difference multiplied by 1000 (e.g. 37 = 0.037).

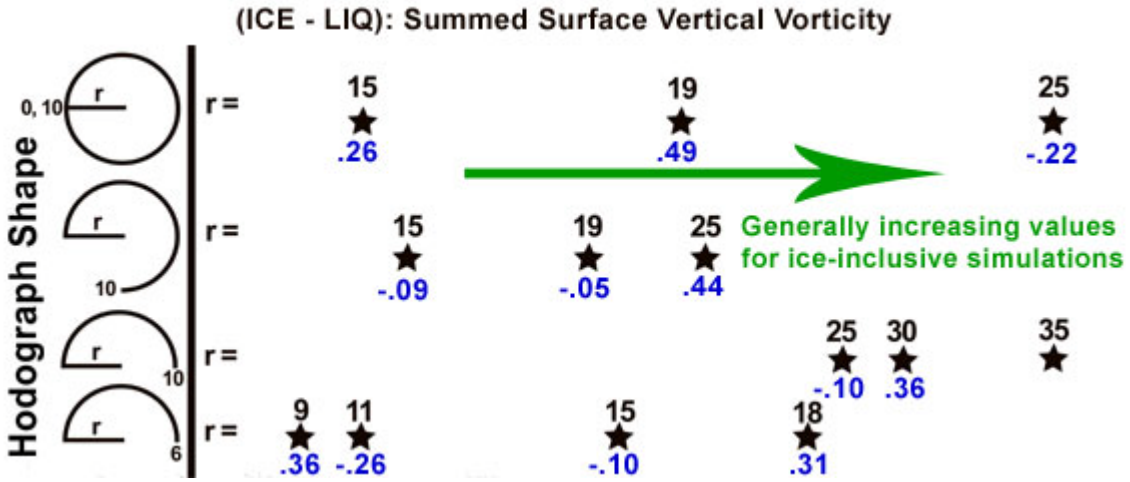

Figure 9: Difference between ice and liquid simulations of maximum surface vertical vorticity summed across all twenty-one model output steps. Blue numbers represent this difference in units of s^{-1}.

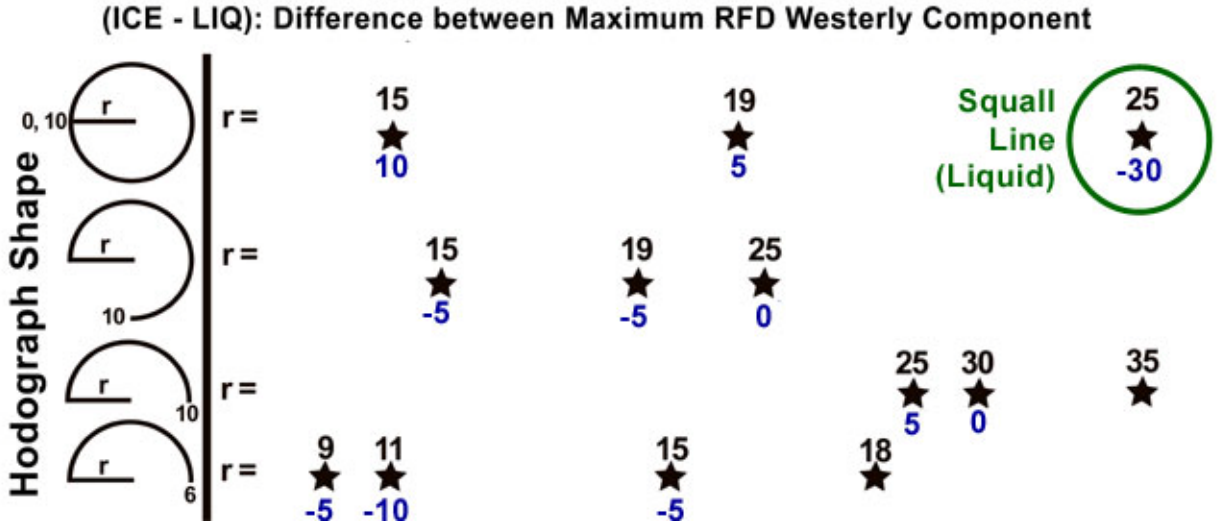

Figure 10: Approximate difference (to the nearest 5 ms^{-1}) between ice and liquid simulations of the strongest westerly component in the RFD at the time of maximum surface vertical vorticity. Blue number represents this difference in ms^{-1}.

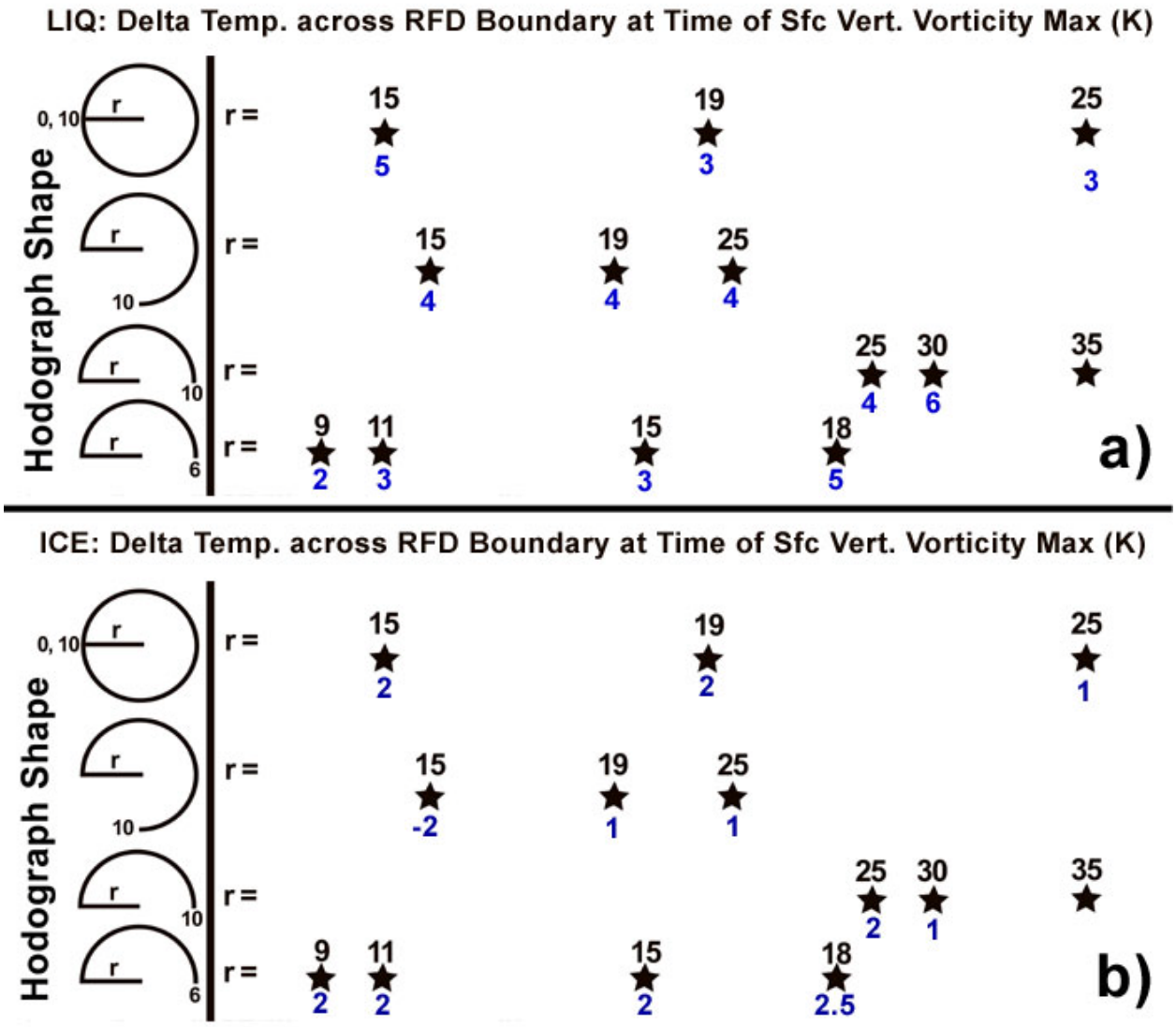

Figure 11: Temperature difference across the RFD boundary, calculated as environmental temperature minus minimum RFD temperature just behind the RFD boundary. (a) is for liquid-only simulations, while (b) is for the ice-inclusive simulations. Blue numbers represent this difference in Kelvin.

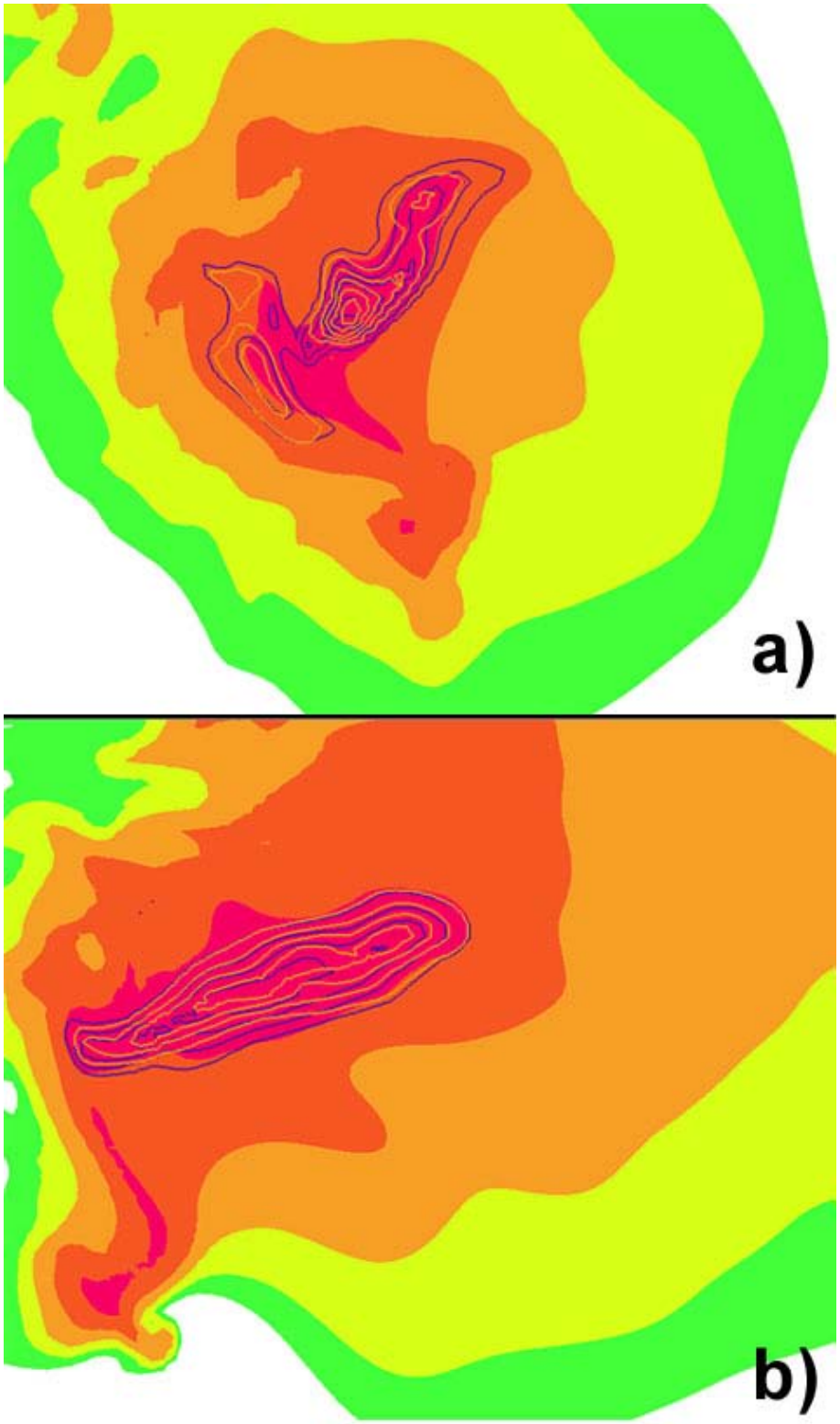

Figure 12: Mixing ratio of hail from graupel (purple contours) and hail from frozen drops (orange contours) for a) a simulation with a full-circle hodograph (I6), and b) a half-circle hodograph (I10). Hail mixing ratio is overlaid on color-filled contours of model-derived reflectivity factor every 10 dBZ beginning with a minimum of 20 dBZ (green contour).

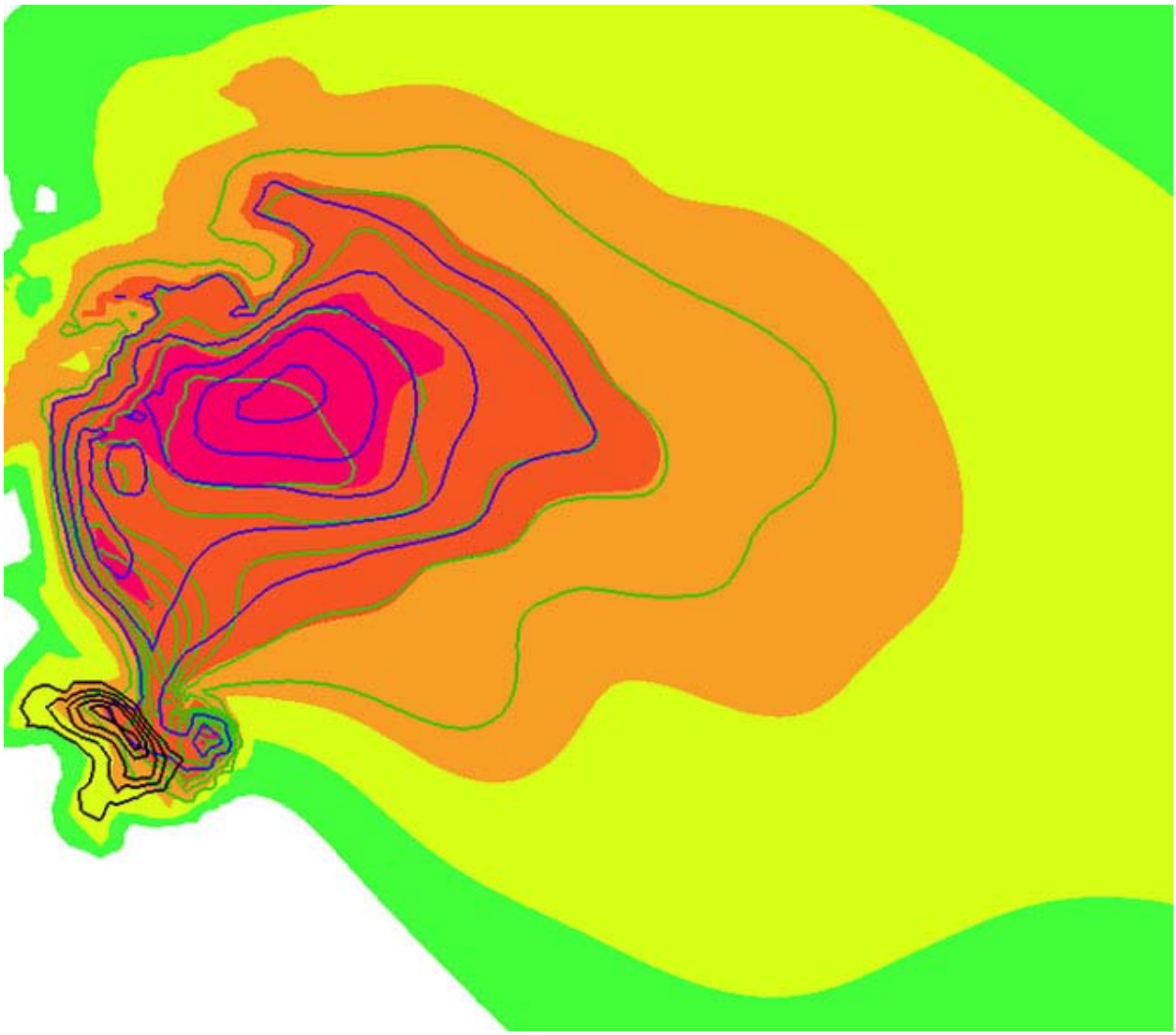

Figure 13: As in Fig. 12, except dark green contours are rain from melting, blue contours are rain from shedding, and black contours are rain formed via warm rain processes.

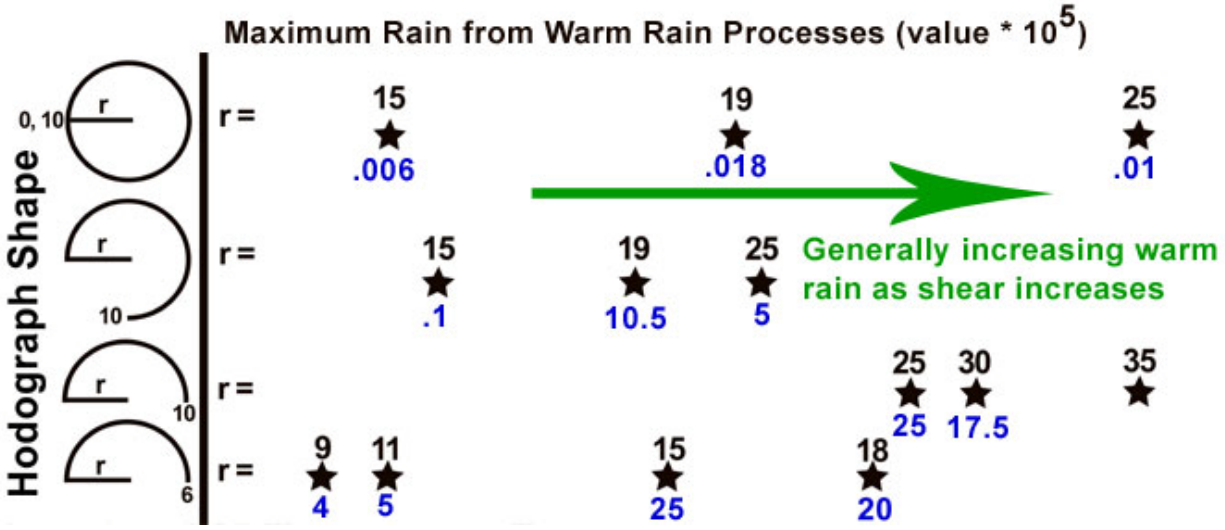

Figure 14: Maximum warm rain mixing ratio at 1000m for the time of maximum surface vertical vorticity in each ice-inclusive simulation. Blue numbers denote this value multiplied by 10^5 for scaling.